Journal of Hazardous Materials, 6 (1982) 129—160
Elsevier Scientific Publishing Company, Amsterdam — Printed in The Netherlands

A COMPARISON OF DENSE GAS DISPERSION MODEL SIMULATIONS WITH BURRO SERIES LNG SPILL TEST RESULTS

D.L. ERMAK, S.T. CHAN, D.L. MORGAN and L.K. MORRIS

Lawrence Livermore National Laboratory, University of California, Livermore, CA 94550 (U.S.A.)

(Received October 16, 1981; accepted November 11, 1981)

Summary

The predictions from three vapor dispersion models for cold dense gas releases are compared with the results from several 40 m^3 LNG spill experiments conducted at China Lake, California, in 1980. The models vary considerably in the degree to which they approximate important physical phenomena and include restricting assumptions. The simplest model (GD), a modified Gaussian plume model, predicted a vapor cloud that was always too high and too narrow by a factor of 1.5 to 3. The second model (SLAB), a layer-averaged conservation equation model with one independent spatial variable (downwind distance), generally predicted the maximum distance to the lower flammability limit (LFL) and cloud width quite well. SLAB assumes the vertical concentration distribution is nearly uniform so that the vertical concentration gradient ($\partial c/\partial z$) is essentially zero from the ground up through most of the cloud and then very steep at the top of the cloud. This was generally not the case in these experiments, especially in the high wind speed tests, where the vertical concentration gradient was found to be more gradual throughout the cloud. The final model (FEM3) is a fully three-dimensional conservation equation model that generally predicted the concentration distribution in time and space rather well. A particular achievement of this model was the prediction of a bifurcated cloud structure observed in one experiment conducted with a low ambient wind speed. Both the SLAB and the FEM3 models accurately predicted the length of time required for the cloud to disperse to a level below the LFL, even in the low wind speed test where the vapor cloud lingered over the source region for a considerable length of time after the LNG spill was terminated.

1. Introduction

Lawrence Livermore National Laboratory (LLNL) is conducting safety research under the sponsorship of the U.S. Department of Energy (DOE) to develop and experimentally verify models to predict the possible consequences of liquefied natural gas (LNG) spills. As part of the DOE program, LLNL and the Naval Weapons Center jointly conducted a series of LNG vapor dispersion experiments in the summer of 1980 at China Lake, California [1,2]. This paper presents a comparison of the predictions from three vapor dispersion models for cold dense gas releases with the results from several of these experiments.

0304-3894/82/0000—0000/$02.75

During the last decade, a number of denser-than-air dispersion models were proposed in the literature [3—9]. Most of the models are based on the classical atmospheric advection-diffusion equation for a neutrally buoyant trace emission with ad hoc modifications to account for density effects. After making the typical approximations, a one-dimensional, Gaussian-plume type model is obtained which conserves the mass of the emitted species but neglects momentum and energy effects. One of the models, SIGMET [9], is based on the complete set of conservation equations for species, mass, momentum, and energy, and is three-dimensional. While this type of model includes a more complete description of the dispersion process, it also is numerically more complex and costly to run on a computer.

In a review on the predictability of LNG vapor dispersion, Havens [10] compares the results from several of these models. He considers a single scenario, namely, that of an instantaneous release of 25,000 m^3 of LNG on water under neutral atmospheric stability conditions, and looks at the model predictions of the maximum downwind distance to the lower flammability limit (LFL). The agreement between models is fairly poor, with the predictions varying by over an order of magnitude.

Recently, a few additional models have appeared in the literature. Chan et al. [11,12] have developed a three-dimensional fluid dynamics model which uses the finite element method to solve the basic conservation equations. Also, a few one-dimensional models [13—16], which attempt to improve the parameterizations in the more important physical processes and include momentum and energy conservation in some average manner, have been developed.

In order to determine the range of conditions for which these models are applicable, detailed data from well-instrumented, large-scale field experiments is needed. A major goal of the DOE program is to help provide this data and the Burro Series of experiments are a significant step in that direction. The concentration data obtained in these experiments has been used to generate contour plots which show the time evolution of the LNG vapor concentration in three-dimensional space [1]. We have made similar contour plots of the results from three dispersion models and present them here in a comparison with the experimental results.

The three dispersion models used in this study are briefly described in the following section and are seen to span the range in complexity from the simple Gaussian-plume type model to the three-dimensional, conservation equation type model. We compare the ability of each model to predict the observed vapor dispersion over the flammable range of fuel—air mixtures, and identify those parts of the models which appear to need improvement. Emphasis is given to those situations where the observed vapor dispersion is most markedly different from that of a neutrally buoyant trace emission.

2. Dispersion models

The three models used in this study are the Germeles—Drake modified Gaussian plume model [7]; a modified version of Zeman's one-dimensional, slab-averaged, conservation equation model [15]; and the fully three-dimensional, conservation equation model of Chan et al. [12]. These models will be referred to as GD, SLAB, and FEM3 respectively and are described in significant detail in the references given above. Here we will only briefly describe each model to clarify the physical basis for each, and the differences between them. In particular, the entrainment and turbulence sub-models are described, due to the dominant role which they play in controlling cloud dispersion.

The Burro tests are closely approximated as spills of constant rate and finite duration. For this type of spill, all of these models treat the source of natural gas (NG) vapor in essentially the same way. The liquid pool of LNG is assumed to be in a steady state with a constant evaporation rate equal to the average spill rate in mass per unit time. The shape of the source area is somewhat different in each model; however, the area is always the same and is given by $A = \dot{V}/W$ where $\dot{V}$ is the volumetric spill rate of LNG and W is the liquid regression rate of evaporation, assumed to be 4.2×10^{-4} m/s. The GD model prediction of the dispersing vapor cloud is not time dependent for this type of spill. The model assumes the spill duration is long enough for the vapor cloud to reach steady state. The other two models are time dependent in this regard and treat the finite duration of the spill explicitly.

The vapor dispersion aspects of each model are described separately below.

2.1 GD model

The GD model is derived from the steady state, Gaussian plume, point source solution to the atmospheric advection—diffusion equation,

$$\frac{\partial c}{\partial t} + U\frac{\partial c}{\partial x} = K_y\frac{\partial^2 c}{\partial y^2} + K_z\frac{\partial^2 c}{\partial z^2}, \tag{1}$$

for the concentration c of the emitted species. Here U is the wind speed (assumed to be constant and in the x-direction) and K_y and K_z are the horizontal and vertical turbulent diffusivities, respectively. Turbulent diffusion in the x-direction is neglected, as it is assumed to be negligible in comparison to the advection of the wind. The turbulent diffusivities are taken to be functions of time since release or, equivalently in this model, functions of the downwind distance x. The GD equation for the concentration of NG vapor is obtained by integrating the point source solution over a finite line source of length L normal to the wind and located a distance x_v upwind of the true source. The result is:

$$c(x,y,z) = \frac{\dot{V}_v}{[2\pi]^{1/2}UL\sigma_z}\cdot\exp\left[\frac{-z^2}{2\,\sigma_z^{\,2}}\right]\cdot\left\{\operatorname{erf}\left[\frac{(L/2)-y}{2^{1/2}\sigma_y}\right] + \operatorname{erf}\left[\frac{(L/2)+y}{2^{1/2}\sigma_y}\right]\right\} \tag{2}$$

where the constant $\dot{V}_v$ is the volumetric source rate of NG vapor at ambient conditions and is approximately 630 times the liquid volume spill rate $\dot{V}$.

The dispersion coefficients σ_y and σ_z are functions of both the downwind distance from the true source x and the virtual source distance x_v, and are related to the turbulence diffusivities (K_y and K_z) by the expression:

$$\sigma^2(x+x_v) = \frac{2}{U} \int_0^{x+x_v} K(x')\,dx' \,. \tag{3}$$

In the GD model, the Pasquill–Gifford dispersion coefficients [17] for continuous ground level sources are used for σ_y and σ_z. These dispersion coefficients are empirically based on atmospheric dispersion experiments of trace emissions. There are six sets of dispersion curves corresponding to six general weather conditions ranging from the most unstable class A to the most stable class F.

The source length L and the virtual source distance x_v are determined by a gravity spread calculation on a cylindrically shaped volume of NG vapor equal to the volume evaporated in the time it takes for the wind to traverse the liquid pool. Initially, the cylindrical cloud is assumed to be pure NG vapor at the boiling temperature and to have a radius equal to the liquid pool radius. The initial height of the cylindrical cloud is $H_i = 2R_i W_v/U$ where W_v is the vapor source velocity which is approximately 250 times the liquid regression rate W. While the properties of the cylindrical cloud are assumed to be homogeneous, the height, radius, temperature, and density change with time due to three processes: gravity spread of the denser-than-air cloud, air entrainment into the cloud, and surface heating of the cloud.

Gravity spread is assumed to increase the cylindrical cloud radius at the rate:

$$\dot{R} = \left[2g\,\frac{(\rho - \rho_a)}{\rho_a} H\right]^{1/2} , \tag{4}$$

where g is the acceleration due to gravity, ρ is the cloud density, and ρ_a is the ambient air density. Air entrainment is assumed to occur only at the top of the cylindrical cloud. It increases the mass and temperature of the cloud and provides an additional source of heat due to the possible condensation and freezing of water vapor by the cold LNG vapor. Together with surface heating, the mass and energy rate equations for the cylindrical cloud are:

$$\dot{M} = \pi\rho_a R^2 w_e \tag{5}$$

$$\dot{E} = \rho_a \pi R^2 C_{pa} T_a w_e + \epsilon_v + \epsilon_w \tag{6}$$

where w_e is the entrainment rate; $M = \pi\rho R^2 H$; $E = MC_p T$; C_p and T are the cloud specific heat and temperature; C_{pa} and T_a are the ambient air specific heat and temperature; ϵ_v is the heat of condensation and freezing of water

$$\frac{\partial V_g}{\partial t} + U\frac{\partial V_g}{\partial x} = \frac{gh}{\rho B}(\rho - \rho_a) - \frac{\rho_a}{\rho}\left(\frac{v_e}{B} + \frac{w_e}{h}\right)V_g - \frac{\rho_s W_s B_s V_g}{\rho B h} - \frac{2\tau_y}{\rho h}, \qquad (11)$$

$$\frac{\partial T}{\partial t} + U\frac{\partial T}{\partial x} = \frac{\rho_a C_{pa}}{\rho C_p}\left(\frac{v_e}{B} + \frac{w_e}{h}\right)(T_a - T) + \frac{\rho_s C_{pn} W_s B_s (T_s - T)}{\rho C_p B h} + \frac{j}{\rho h C_p}, \qquad (12)$$

$$\frac{\partial B}{\partial t} + U\frac{\partial B}{\partial x} = V_g + v_e. \qquad (13)$$

The above equations, together with the ideal gas approximation for the equation of state and specific heat (see eqns. (20) and (21)) form the SLAB model. The main cloud variables are the cloud height h and half-width B, the layer-averaged density ρ, mass fraction ω, velocity in the direction of the wind U, temperature T, and the crosswind cloud velocity at the side edges V_g. The bar over a quantity to designate a layer-average has been dropped since it is understood that all quantities are averaged in this manner. The remaining parameters are the acceleration due to gravity g; the NG source velocity W_s and source half-width B_s; the specific heat C_p; the molecular weight M; the vertical and horizontal entrainment rates w_e and v_e; and the surface momentum and heat fluxes τ and j. The subscripts "s", "a", and "n" designate an NG source-related property, an ambient air property, and an NG vapor property respectively.

The entrainment rate equations have been modified from those proposed by Zeman [15]. The vertical entrainment rate is taken to be a density-weighted combination of an ambient air entrainment rate and a stably stratified dense layer entrainment rate [18] and is:

$$w_e = \frac{\pi^{1/2} k U_{a*}(\rho_s - \rho)}{\phi_a(\rho_s - \rho_a)} + \frac{2.5\rho_a U_*^3}{g(\rho_s - \rho_a)h}, \qquad (14)$$

$$\text{where } \phi_a = \begin{cases} (1 - 16\,Ri)^{-1/4}, & Ri \leqslant 0; \\ 1 + 5\,Ri, & Ri > 0; \end{cases}$$

Ri is the ambient Richardson number; k is von Karman's constant; $U_* = c_f U$; and c_f is a friction constant (found to be approximately 0.038 at China Lake). A comparison of the two terms shows the second term to be much less than the first, except when $\rho \sim \rho_s$ or $h \sim 0$. The second term is generally quite small so that the effect of increased density in this model is to reduce the rate of air entrainment into the cloud.

The horizontal entrainment rate is

$$v_e = (1.8)^2 (h/B) w_e . \qquad (15)$$

The rationale for the ratio factor (h/B) is based on the assumption that in the source region or whenever the cloud is low and flat (i.e., $h \ll B$), horizontal entrainment will do little to dilute the cloud. As the cloud disperses

and becomes more dilute, gravity spread decreases and entrainment becomes the dominant dispersal mechanism. At sufficiently far downwind distances, h and B become proportional to w_e and v_e, respectively, and then $v_e \doteq 1.8\, w_e$. This result reflects the empirical observation that the horizontal and vertical standard deviations for both the wind speed and the spread of a trace emission in the atmosphere are approximately proportional by this factor.

The six coupled, non-linear partial differential equations (PDE) of the SLAB model are solved using the PDECOL [19] computer software package. PDECOL uses finite element collocation methods based on piecewise polynomials for the spatial discretization techniques and standard implicit methods for the time integration. To improve numerical stability, a diffusion term with a coefficient of about 1 m^2/s was added to each PDE. The main effect of this term on the model predictions is to smooth the leading and trailing edges of the cloud.

2.3 FEM3 model

In the FEM3 model, the dispersion of NG vapor is predicted by solving the three-dimensional conservation equations for the mean (time-averaged) quantities in a turbulent flow field. A generalized anelastic approximation, adapted from Ogura and Philips [20], is used to accommodate large density changes in both time and space while precluding sound waves. The result is the following form for the conservation equations of mass, momentum, energy, and species:

$$\nabla \cdot (\rho \boldsymbol{u}) = 0\,, \tag{16}$$

$$\frac{\partial(\rho \boldsymbol{u})}{\partial t} + \rho \boldsymbol{u} \cdot \nabla \boldsymbol{u} = -\nabla p + \nabla \cdot (\rho K^{\mathrm{m}} \cdot \nabla \boldsymbol{u}) + (\rho - \rho_{\mathrm{h}})\boldsymbol{g}, \tag{17}$$

$$\frac{\partial \theta}{\partial t} + \boldsymbol{u} \cdot \nabla \theta = \nabla \cdot (K^{\theta} \cdot \nabla \theta) + \frac{C_{\mathrm{pn}} - C_{\mathrm{pa}}}{C_{\mathrm{p}}} (K^{\omega} \cdot \nabla \omega) \cdot \nabla \theta + S\,, \tag{18}$$

$$\frac{\partial \omega}{\partial t} + \boldsymbol{u} \cdot \nabla \omega = \nabla \cdot (K^{\omega} \cdot \nabla \omega)\,. \tag{19}$$

These equations, along with the ideal gas law approximation for the density and the specific heat,

$$\rho = \frac{M_{\mathrm{n}} M_{\mathrm{a}} P}{RT[M_{\mathrm{n}} + (M_{\mathrm{a}} - M_{\mathrm{n}})\omega]} = \frac{MP}{RT}, \tag{20}$$

$$C_{\mathrm{p}} = C_{\mathrm{pa}}(1-\omega) + C_{\mathrm{pn}}\,\omega, \tag{21}$$

are the main governing equations. Here $\boldsymbol{u} = (u,v,w)$ is the velocity; ρ is the density of the mixture; p is the pressure deviation from an adiabatic atmosphere at rest with corresponding density ρ_{h}; g is the acceleration due to

gravity; θ is the potential temperature deviation from an adiabatic atmosphere; S is the temperature source term (e.g., latent heat); ω is the mass fraction of NG vapor; and K^{m}, K^{θ} and K^{ω} are the diagonal eddy diffusion tensors for the momentum, energy, and NG vapor, respectively. In the equation of state, P is the absolute pressure, R is the universal gas constant, T is the absolute temperature ($T/(\theta+\theta_0) = (P/P_0)^{R/MC_{\mathrm{p}}}$), and M is the suitably averaged molecular weight of the mixture. As before, subscripts "n" and "a" denote NG and air, respectively.

The main step in developing the generalized anelastic approximation is to replace the continuity equation, $\nabla \cdot (\rho u) = -\partial\rho/\partial t$, with eqn. (16). The variation of density with time is then determined implicitly by the time variation of temperature, pressure, and composition via the ideal gas law, eqn. (20). The anelastic approximation is very similar to the incompressibility approximation, $\nabla \cdot u = 0$, for constant density flows. In both cases, compressibility effects are assumed to be negligible since the Mach number is always very small (generally $\leqslant 0.05$ for LNG simulations) and therefore acoustic waves are assumed to be unimportant and can be filtered a priori.

Turbulent diffusion in this model is treated by using a K-theory approach in which the turbulence level is modified by the cold, dense cloud in high concentration regions, yet approaches ambient levels as the cloud becomes more dilute. The three diffusivity tensors are assumed to be diagonal and equal with different elements for the vertical and horizontal directions. The vertical diffusion coefficient K_{v} is expressed as the sum of two terms,

$$K_{\mathrm{v}} = K_{\mathrm{a}}(1-\omega) + K_{\rho}\omega \ , \tag{22}$$

where K_{a} is the ambient vertical diffusivity and K_{ρ} is a dense-layer diffusivity. The horizontal diffusivity K_{H} is simply taken to be 6.5 times as large as the vertical diffusivity.

The ambient atmospheric conditions are characterized by the diffusivity

$$K_{\mathrm{a}} = \frac{k\, U_{\mathrm{a}*} z}{\phi_{\mathrm{a}}} \quad \text{where} \quad \phi_{\mathrm{a}} = \begin{cases} (1-16Ri)^{-1/4}, & Ri \leqslant 0 \ , \\ 1+5Ri \qquad\ , & Ri > 0 \ , \end{cases} \tag{23a}$$

and the wind velocity profile

$$U_{\mathrm{a}} = \frac{U_{\mathrm{a}*}}{k}(\ln z/z_0 - \psi_{\mathrm{a}}) \quad \text{where} \quad \psi_{\mathrm{a}} = \begin{cases} 1.1(-Ri)^{1/2}, & Ri \leqslant 0 \ , \\ -5\,Ri \qquad\ , & Ri > 0 \ . \end{cases} \tag{23b}$$

Here k is von Karman's constant; $U_{\mathrm{a}*}$ is the ambient friction velocity; Ri is the ambient Richardson number; and it is assumed that $Ri = z/L$ where L is the Monin—Obukhov length. The ambient wind velocity profile is approximated in the finite element code by a quadratic and by using a specified shear stress boundary condition at $z = 0$ to avoid the need for an excessively fine grid to resolve the logarithmic function near the ground. The ambient diffusivity is also modified near the ground by replacing z in eqn. (23a) with $z + z_{\mathrm{j}} e^{-z/z_{\mathrm{j}}}$

where z_j is a constant whose value is determined by requiring the ambient vertical momentum flux, $\rho_a K_a (\partial U_a/\partial z)$, at the ground to be $\rho_a U^2_{a*}$. In the Burro simulations the quadratic wind profile fit was made using the average velocity data at the 1, 3, and 8 m heights, and the value of z_j was calculated to be about 1.4 m.

Two sub-models for K_ρ are used in this study. One is a Richardson number diffusivity for a stably stratified density layer that is similar to the dense-layer entrainment rate used in the SLAB model and is given by

$$K_\rho = K_{\rho r} = \frac{1.25\,\rho U_*^3}{g(\rho - \rho_a)}, \tag{24}$$

which tends to reduce the turbulence level from the ambient value in high NG concentration regions. The other model is a mixing length model given by

$$K_\rho = K_{\rho m} = \frac{\rho_a}{\rho} \frac{K_a}{\dfrac{\partial U_a}{\partial z}} \left[\sum_{i,j}^{3} \left(\frac{\partial U_i}{\partial x_j}\right)^2\right]^{1/2}, \tag{25}$$

where the turbulence level is proportional to the overall shear. Both sub-models were used in each simulation; however, the results were essentially identical (except in Burro 8 where the $K_{\rho m}$ sub-model appeared to work better) so only results obtained with the latter sub-model will be presented.

The main governing equations, eqns. (16—21), along with those for the sub-models, are solved numerically with appropriate initial and boundary conditions. Equations (16—19) are spatially discretized by the finite element method in conjunction with the Galerkin method of weighted residuals. The time integration scheme is basically the explicit forward Euler method except for pressure which must be computed implicitly.

2.4 Model comparisons

The three models differ considerably in their approach to simulating the atmospheric dispersion of a cold, dense-gas release. Perhaps the most obvious differences are related to the degree to which each model incorporates the basic conservation laws and three-dimensional effects. The GD model is based on the single conservation of species equation and neglects momentum and energy effects after the initial gravity spread calculation to determine the vapor cloud dimensions at the source. On the other hand, the SLAB model includes the conservation equations of mass, momentum, and energy, in addition to the species equation, but only in an average way. Variations in the crosswind plane are neglected, and all properties of the vapor cloud are expressed as crosswind averages which vary in the downwind direction only. The FEM3 model includes the most complete description of the conservation laws by treating them explicitly in three dimensions.

A unique feature of the SLAB model is that it calculates only crosswind-

averaged properties, and characterizes the cloud shape by the height, h, and half-width, B. The parameters B and h do not correspond to any particular concentration level. Rather, they can be considered to describe a surface which encloses the bulk of the cloud, for example 90%. Consequently, the crosswind concentration distribution is not specified, although it was assumed to be nearly uniform, and it is difficult to compare the predicted cloud shape from this model with the contour plots obtained from the experiments. To overcome this difficulty, we have assumed the following distribution for the vapor cloud concentration:

$$c(x,y,z) = c(x)\cdot\{1 - [2y/3B(x)]^2\}\cdot\{1 - [2z/3h(x)]^2\}, \qquad (26)$$

where $c(x)$ is the layer-averaged concentration expressed as the volume fraction and $c(x,y,z)$ is zero for $z > 3h/2$ and $|y| > 3B/2$. The use of eqn. (26) allows for the calculation of concentration contour plots which are based on the average concentration and the cloud height and width. While the choice of a quadratic distribution is arbitrary, it is somewhat consistent with the assumption of near uniformity. It should be noted that the maximum distance to the LFL (or any other concentration level) is not affected by the use of eqn. (26) since it is applied after the average properties are calculated.

There are other important differences and these are related to the manner in which each model treats the effects of gravity and turbulence. As noted above, the GD model treats gravity spreading of the denser-than-air cloud only in the calculation of the vapor cloud height and width at the source. Gravity effects are totally neglected after this initial calculation. The downwind dispersion of the vapor cloud is assumed to be due to atmospheric turbulence and is governed by empirical coefficients for a neutrally buoyant trace emission. In contrast to this, the SLAB and FEM3 models treat the effects of gravity continuously throughout the calculation. This is done in the FEM3 model by solving the three momentum conservation equations at each point, while the SLAB model solves two layer-averaged momentum equations and uses the hydrostatic approximation.

These two latter models differ considerably in their approach to turbulence. The SLAB model uses the somewhat artificial concept of entrainment across the cloud—air interface and essentially neglects any explicit treatment of turbulence within the vapor cloud. Air is entrained into the cloud at the surface and then is assumed to mix rapidly in the cloud creating a nearly uniform layer in the crosswind plane. Thus, there are two separate regions: the cloud and the ambient atmosphere. Mixing between the two is assumed to occur at the interface and is governed by an entrainment velocity which depends on the local properties of both the cloud and the surrounding atmosphere. The FEM3 model assumes that turbulence can be described as a diffusion process and uses a continuous diffusion coefficient which depends on the local properties of the LNG vapor—air mixture. While the entrainment and diffusion concepts are peculiar to the SLAB and FEM3 models respectively, the choice of a particular entrainment or diffusion sub-model is not

an essential aspect of the models. Several sub-models have been proposed in the literature and could be used without changing the whole model.

3. Burro LNG spill tests

The Burro series of experiments included eight LNG dispersion tests with spill volumes of up to 40 m^3 and spill rates of up to 20 m^3/min. The experiments were initialized by spilling the LNG onto the surface of a 1 m deep water pond. The LNG exits from a 25 cm diameter pipe about a meter above the surface of the pond, flowing straight down. Approximately 2 cm below the water surface, the LNG stream encounters a steel plate which directs it radially outward along the surface of the water. The spill pond is only about 58 m in diameter; consequently, while the spill is onto water, most of the dispersion occurs over land.

Ground level immediately surrounding the pond is about 1.5 m above the water level. Downwind of the pond, the terrain rises at the rate of about 7° to a height of 7 m above the water level at a distance of 80 m and remains relatively flat thereafter. Looking downwind from the spill point, the terrain slopes slightly ($\lesssim 1°$), rising to the left and dropping to the right. There is a gully just beyond the right side of the instrumentation array that drops to an elevation of about 4—6 m below the centerline of the array. The effect of terrain on the dispersion of the LNG vapor is difficult to quantify, although it is quite apparent in Burro 8 and is discussed further in the following sections.

Model predictions are compared with four of the experiments: Burro 3, 7, 8, and 9. A summary of the test conditions for each of these experiments is given in Table 1. At China Lake, the roughness length, z_0, and the friction

TABLE 1

Summary of Burro test conditions

	Burro 3	Burro 7	Burro 8	Burro 9
V (m^3)	34.0	39.4	28.4	24.2
$\dot{V}$ (m^3/min)	12.2	13.6	16.0	18.4
U_2 (m/s)	5.4	8.4	1.8	5.7
T_2 (°C)	34.0	34.0	33.0	35.0
T_* (°C)	−0.65	−0.23	+0.145	−0.10
Stability	C	D	E	D
K_2 (m^2/s)	0.29	0.32	0.037	0.21

Definitions

V	LNG volume spilled
$\dot{V}$	Mean LNG spill rate
U_2	Mean wind speed at 2 m height
T_2	Mean temperature at 2 m height
T_*	$\partial T/\partial(\ln z)$
Stability	Estimated Pasquill—Gifford stability class
K_2	Momentum diffusivity at 2 m height

constant, c_f, defined as the ratio of the friction velocity, U_*, to the wind velocity at 2 m height, were found to be nearly constant and had average values of $z_0 = 2.05 \times 10^{-4}$ m and $c_f = 0.038$. The estimated Pasquill—Gifford atmospheric stability class, used in the GD model calculations, is based on the methods proposed in Turner [21] and by Golder [22]. The method for calculating the momentum diffusivity, along with a more detailed description of the ambient atmospheric conditions, is given in [2].

Instrumentation for measuring the concentration of the NG vapor cloud as it dispersed downwind were located in four arcs at 57 m, 140 m, 400 m, and 800 m downwind of the spill point. There were about seven stations in each arc and the NG vapor concentration was measured at three heights (1 m, 3 m, and 8 m) at each station. In these tests, the 5% volume fraction level, corresponding approximately to the lower flammability limit (LFL), was generally within or just slightly beyond the 400 m arc.

Measurements of the heat transfer from the ground were also made during the passage of the cold NG vapor cloud. A simple heat transfer model

$$\Delta H = V_H \rho C_p \Delta T_1, \tag{27}$$

was investigated where ΔH is the ground heat flux to the cloud, ΔT_1 is the temperature decrease from ambient at 1 m height, and V_H is an effective heat transfer velocity. Several models for V_H, including ones using velocity and buoyancy terms, were used to fit the data. However, the best fit was obtained by using the constant value of $V_H = 0.0125$ m/s and this value is used in the model calculations.

4. Comparison of Burro results with model predictions

In comparing the model calculations with experimental results, consideration must be given to the time duration over which the data is to be averaged since the models only calculate time-averaged or ensemble-averaged quantities. Here we compare the model results to concentration data from the Burro experiments that have been averaged using a 10 s moving average. This time interval was chosen somewhat arbitrarily; the intent was to use an averaging time that is long enough to smooth out short-wavelength (much less than cloud width) fluctuations, but short enough to preserve cloud meander. Even with this averaging, the experimental concentration contours tended to fluctuate with time. Since the main interest in this work is related to safety, we generally emphasize the maximum extent of the concentration contours and, in particular, the maximum extent of the flammable region. Regarding fluctuations about the 10 s average, peak concentrations of 5% (LFL) or greater were commonly observed when the 10 s average concentration was less than 5%, but were almost never observed when it was less than 1% [2].

The 10 s average concentration data was linearly interpolated in space to generate concentration contour plots at 10 s intervals. Obviously, there is an uncertainty in the location of the experimental contours which depends

on the distance between measurements. Within a row of instruments, the interpolation uncertainties are believed to be less than a meter in the vertical and only a small fraction of the instrument spacing in the horizontal. The interpolation uncertainties between rows of instruments are considerably greater since the distance between rows is larger. The maximum extent of the 5% contour (X_{LFL}) was generally located between the 140 m and 400 m rows where the interpolation uncertainty in X_{LFL} is estimated to be approximately −40 to +20 m. These estimates were obtained from investigations involving a number of tests [2].

4.1 Burro 3

In this comparison, Burro 3 is unique in that it is the only case in which all three models underestimate the maximum distance to the LFL (X_{LFL}) as determined by the contour plots of the experimental data. This is shown in Table 2 where X_{LFL} is given for all four experiments and for each model simulation. The SLAB and FEM3 models underestimate X_{LFL} by 40 and 65 m respectively, and the GD model underestimates it by 130 m. In addition, the predicted cloud behavior of the SLAB and FEM3 models over the duration of the test was considerably different to that observed in the experiment.

TABLE 2

Maximum downwind extent of the LFL (m)

	Expt.*	GD	GD+	SLAB	FEM3
Burro 3	255	126	190	215	190
Burro 7	200	150	212	264	210
Burro 9	325	235	344	315	330
Burro 8	420	661	1150	418	630

*The estimated uncertainty in the experimental value is −40 to +20 m.

The duration of the Burro 3 spill was 167 s, which is long enough that one might expect the resultant vapor cloud to set up a quasi-steady state (as predicted by the SLAB and FEM3 models) at least within the 5% concentration level. However, the contour plots of the field data show a different behavior. As expected, X_{LFL} initially increases as the cloud develops. Between 60 and 120 s from the time the spill began, X_{LFL} oscillates between 215 and 255 m. After 120 s and for the next 100 s, X_{LFL} decreases to a value of 120—140 m. Also during this latter period, the vapor cloud is bifurcated for about 45 s. The reason for this change in cloud shape is thought to be related to a local reduction in the wind speed in the vicinity of the spill pond, but is not completely understood.

Nor can it be fully explained why the maximum X_{LFL} value during the first

half of the spill is so much greater than the model predictions. Several possible explanations as to why the models underestimated X_{LFL} in only this experiment have been investigated. For example, changes in the LNG spill rate were checked but found to be too small to account for the large value of X_{LFL}. The effect of inoperative stations on the contour plots was also investigated; however, if there was any effect, it would tend to reduce X_{LFL} because of missing peak concentrations. The largest discovered uncertainty in the experimental value of X_{LFL} is due to interpolating the concentration between the 140 m and 400 m rows. If this is considered, the SLAB model prediction of X_{LFL} is within the lower limit of the experimental value and the FEM3 result is just below it.

As seen in Table 2, the GD estimate of X_{LFL} is significantly lower than either of the other two models. One might suggest that it is more appropriate to use a higher stability class in the GD simulations since the model predictions are being compared to 10 s average concentrations and the Pasquill–Gifford dispersion coefficients were designed for 10 min or longer averages. For this reason, a second GD run was made for each experiment with the stability increased by one class. The results are shown in Table 2 under the GD+ heading. An increase in stability is seen to improve the X_{LFL} estimates for the high wind speed, less stable cases (Burro 3, 7, and 9); however, it leads to an overestimate of X_{LFL} by more than a factor of two in the low wind speed, stable case of Burro 8.

The downwind distance to the LFL is only one measure of the models' ability to simulate the experiments. A better evaluation can be made by comparing the location and shape of the LFL contour and, in general, by comparing a range of contours which show the overall concentration distribution. Such a contour plot is shown in Fig. 1(a) where crosswind concentration contours 57 m downwind are plotted at a time of 100 s. The uncertainty in the location of these contours is much less than the uncertainty in X_{LFL} since the distance between instruments is much less. Also shown in Fig. 1 are the model predictions, which include only half the distribution since they assume the cloud is symmetric about the cloud centerline. The scale in each of the plots is identical, and the experimental contours have been translated along the crosswind axis so that they are roughly centered within the plot.

As can be seen in Fig. 1, the contours from the FEM3 calculation are in very good agreement with those generated from the experimental data. The SLAB model appears to predict the overall height and width of the cloud fairly well, especially if one considers the 5% contour as representative of the overall cloud dimensions. However, the 1% contour is significantly lower than in the experiment, and the 15% contour is both higher and wider. This suggests that the quadratic function used in eqn. (26) for the concentration distribution is not the most appropriate, especially in the vertical direction.

The GD model is seen to predict a cloud which is too high and too narrow. The GD 5% contour is about twice as high and nearly half as wide as in the experiment. Also shown in Fig. 1(c) is a GD simulation in which the stability

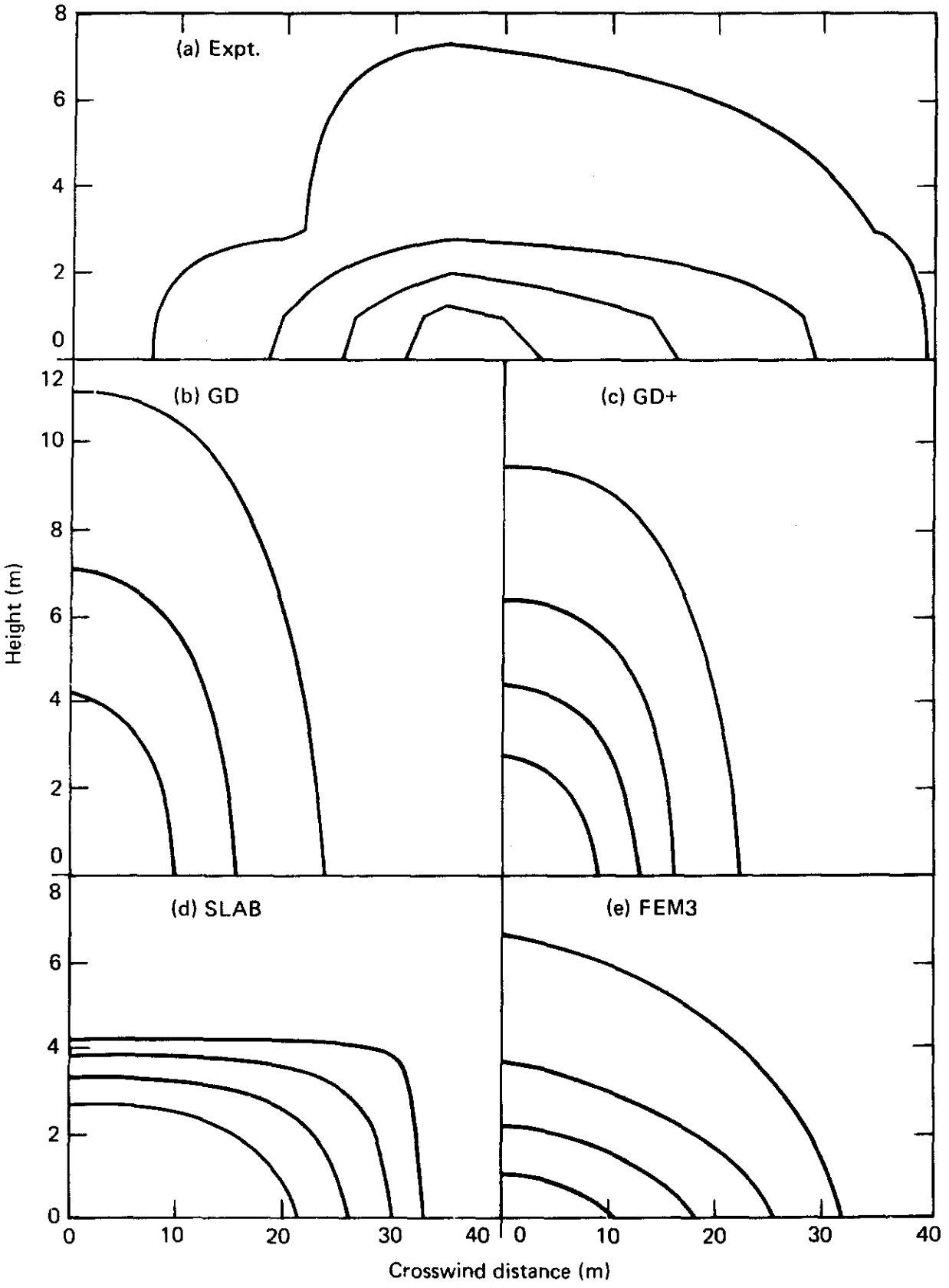

Fig. 1. Burro 3 crosswind contour plots of cloud concentration 57 m downwind at t = 1 00 s. Experimental contour plot shows full cloud width while model results show only half-width. Contour lines designate 1, 5, 10 and 15% levels and vertical to horizontal distance scale is 1 to 4.

class is increased by one from that given in Table 1. While this change in stability improved the prediction of X_{LFL} (see Table 2), it did little to improve the shape of the cloud, it is still too high and too narrow. This characteristic of the GD model was found to hold for each of the Burro experiments used in this study.

4.2 Burro 7

The Burro 7 spill rate and duration were quite similar to that of Burro 3, but the wind speed was about 60% higher and the atmospheric stability was estimated to be one class higher. The wind direction took the cloud along the edge of the instrumentation array as it moved downwind and the cloud centerline extended beyond the edge of the array during much of the spill. The cloud meandered over the array three times, and each time a maximum X_{LFL} value of 190—200 m was calculated. As can be seen in Table 2, the FEM3 estimate of X_{LFL} was in good agreement with this value. The SLAB model overestimates X_{LFL} by about 60 m, while the GD model underestimates it by about 50 m. These last two estimates are not too far outside the uncertainty limits of the experimental value due to the interpolation between the 140 m and 400 m rows.

In Fig. 2 a contour plot of the cloud concentration observed in the experiment at the first row of instruments and t = 140 s is compared to similar plots from the SLAB and FEM3 models. The model results do not compare very well with experiment in this row. The experimental cloud is bifurcated, which the models do not predict, and is wider than the simulated clouds. For example, the 1% contour in the experimental contour plot is 72 m wide, while it is about 45 and 55 m wide in the SLAB and FEM3 plots respectively.

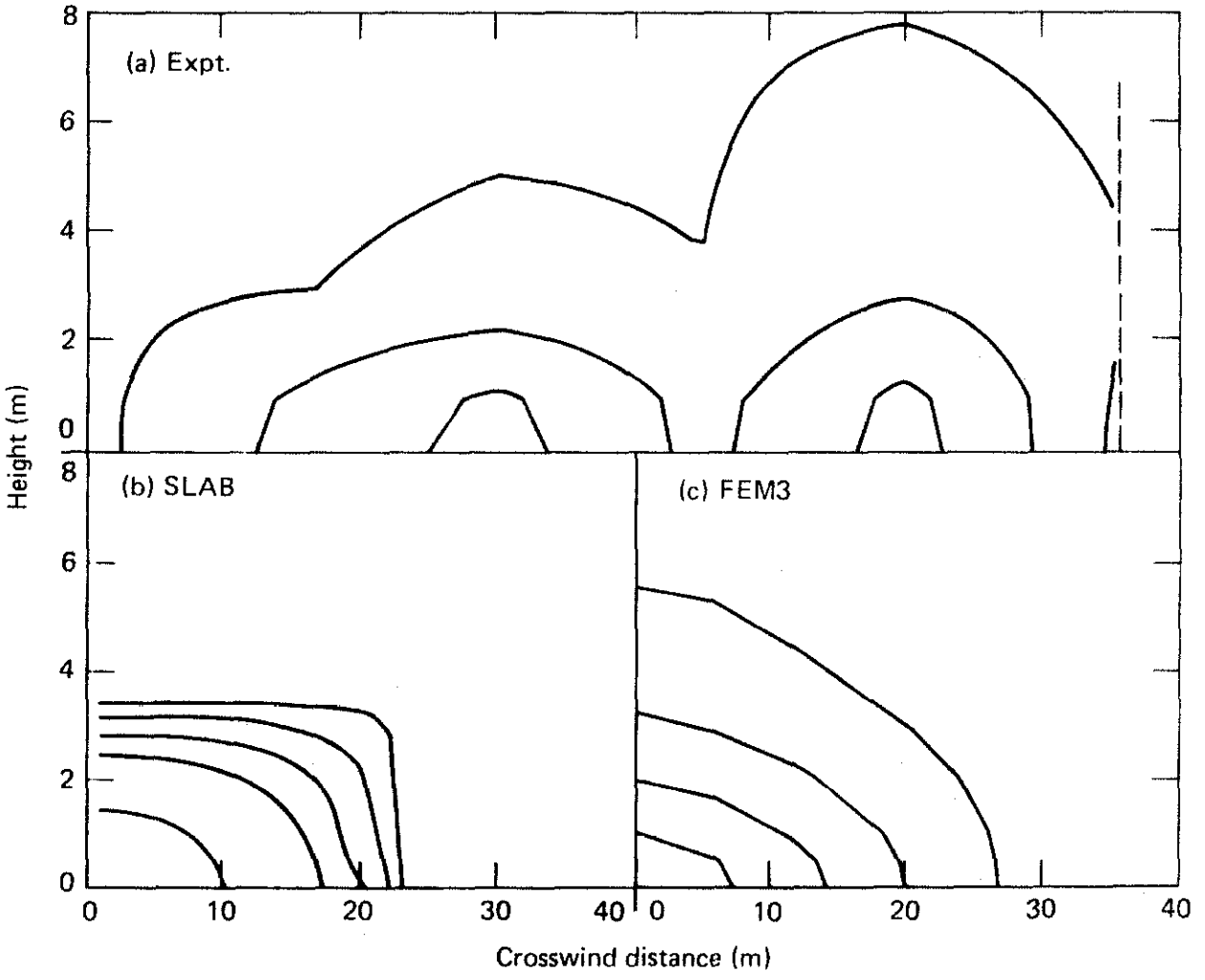

Fig. 2. Burro 7 crosswind contour plots of cloud concentration 57 m downwind at t = 140 s. Dashed line in plot (a) indicates outer edge of instrument array. Contour lines designate 1, 5, 10, 15, and 25% levels and vertical to horizontal distance scale is 1 to 4.

The models also predict significantly higher concentrations. The maximum concentration observed in this row in the experiment was about 12%, while it was over 25% in the SLAB result and about 17% for the FEM3 result.

The models do significantly better in the second row 140 m downwind, as can be seen in Fig. 3. In particular, the FEM3 model does very well. The 1% contour is 80 m wide and 6.5 m high in the experimental plot and 68 m wide and 7.2 m high in the FEM3 result. Similarly, the 5% contour is about 40 m wide and 2.2 m high in both plots. The SLAB model prediction of the cloud height and width as given by the 1% contour is in fair agreement with experiment at this downwind distance also. It still predicts too high a maximum concentration, as would be expected since it overestimates X_{LFL}. Perhaps a more important difference between the SLAB and experimental plots is the vertical concentration gradient. In the SLAB result, the 5% contour is more than twice as high as in the experimental plot, while the 1% contour is somewhat lower than that in the experiment. This discrepancy in the vertical gradient between the SLAB model and the experimental results was observed in all the higher wind speed cases (Burro 3, 7, and 9).

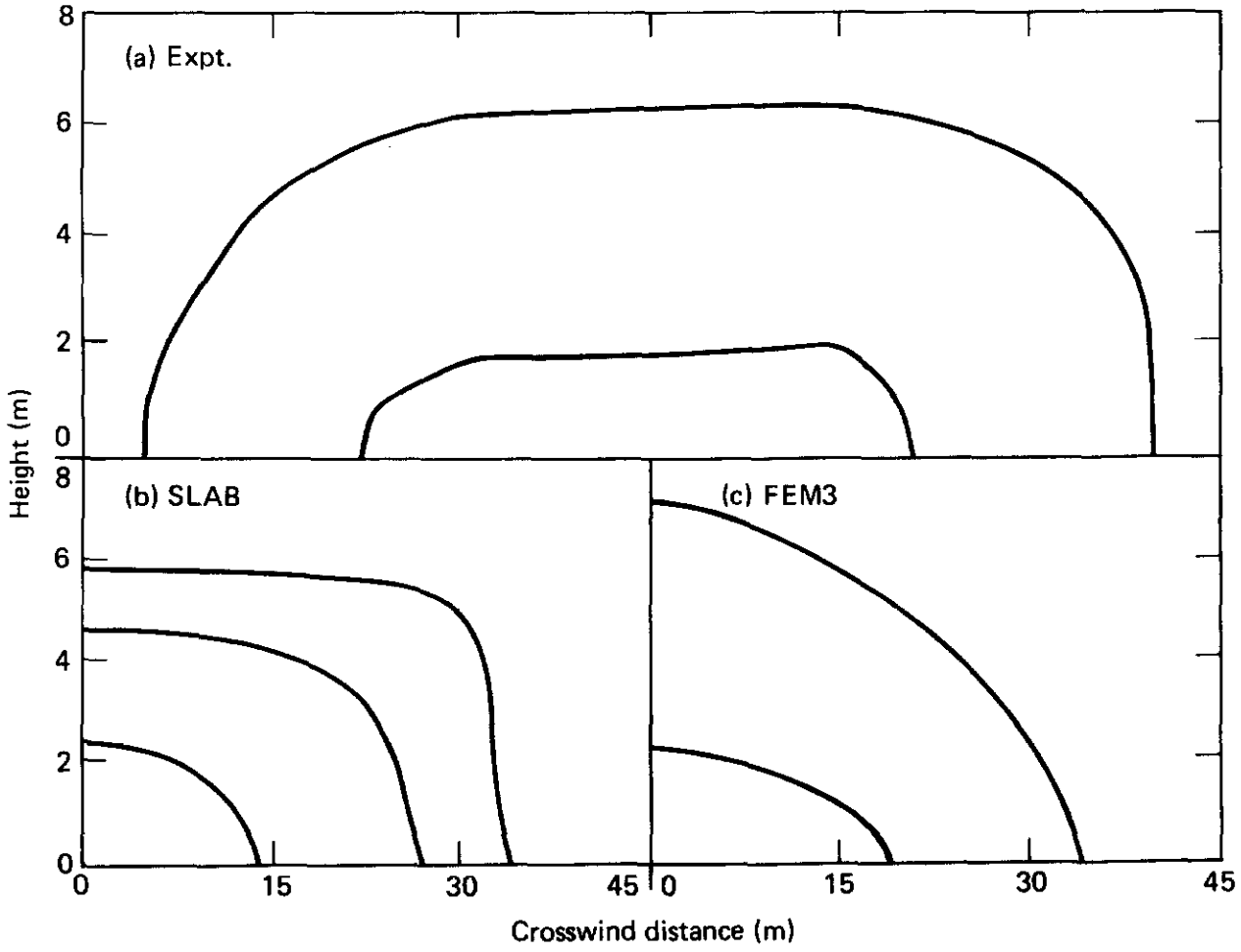

Fig. 3. Burro 7 crosswind contour plots of cloud concentration 140 m downwind at t = 160 s. Contour lines designate 1, 5 and 10% levels and vertical to horizontal distance scale is 1 to 4.

4.3 Burro 9

Burro 9 had the highest spill rate of all the Burro experiments and was conducted under a fairly high wind speed, as were Burro 3 and 7. A series of

rapid-phase-transition (RPT) explosions occurred during this experiment and, as a consequence, the spill was terminated after only 79 s. The RPTs threw enough water and mud on the first row of instruments to render the infrared gas sensors inoperable for most of the test. Figure 4(a) shows a horizontal contour plot of the cloud concentration at a height of 1 m just after the spill was terminated. The maximum X_{LFL} value of 325 m was obtained in the experimental contour plots at this time; however, this value may be larger than the actual value by about 25 to 40 m as a result of interpolation uncertainties. The value of X_{LFL} jumped up to 325 m just as the leading edge of the cloud reached the 400 m row and then rapidly fell to a value below 250 m after the spill valve was closed. In the two 10 s intervals before this, X_{LFL} was 275 and 285 m, respectively.

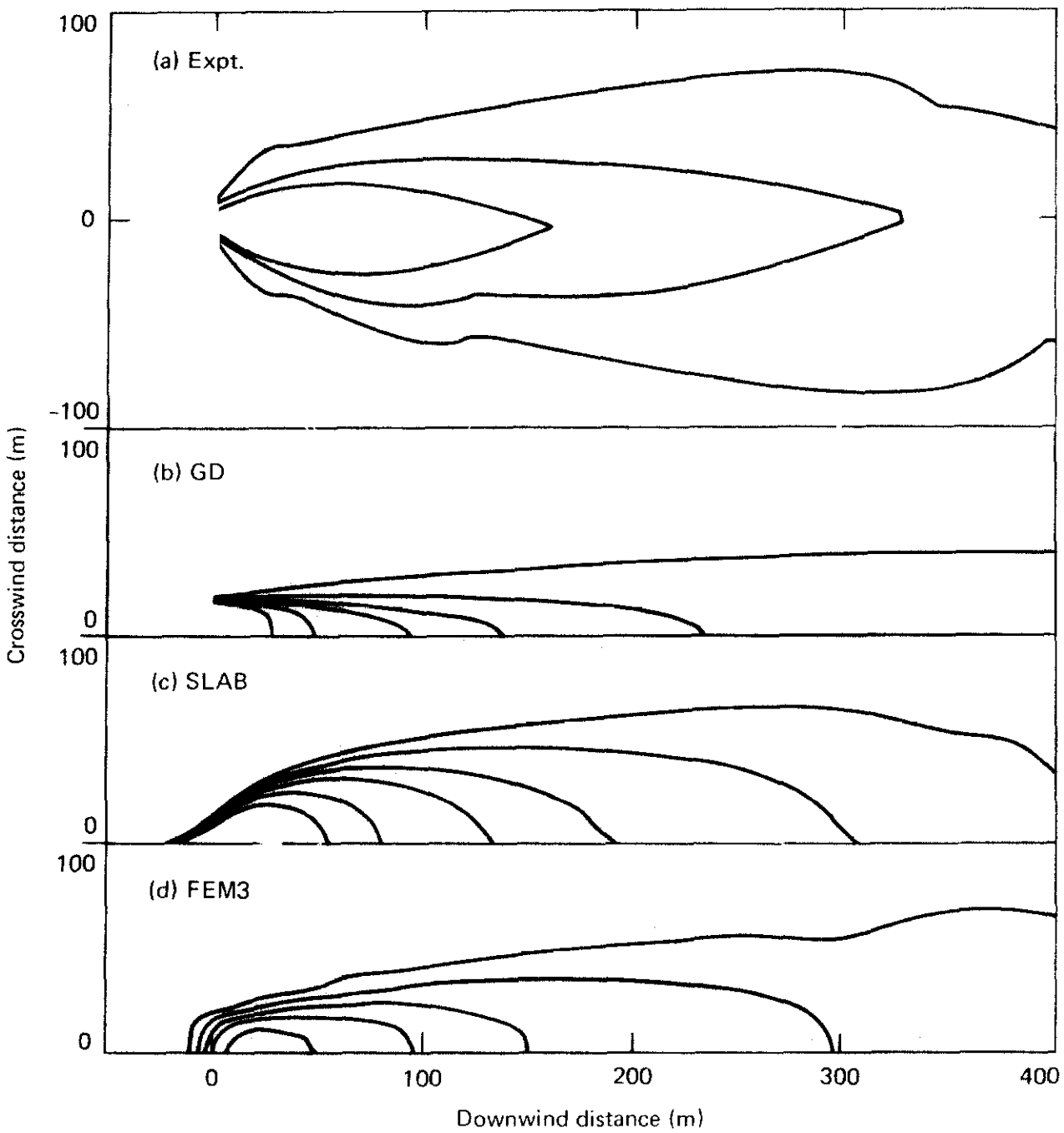

Fig. 4. Burro 9 horizontal contour plots of cloud concentration 1 m above ground at t = 80 s. Experimental contour plot shows full cloud width while model results show only half-width. Data from first row of instruments was excluded from experimental plot since these measurements were degraded by RPT explosions. Contour lines designate 1, 5, 10, 15, 25, and 35% contours and crosswind to downwind distance scale is 1 to 1.

Also shown in Fig. 4 are the corresponding contour plots from each of the three models. At the time of this plot, the SLAB and FEM3 results for X_{LFL} have not reached their maximum value. The maximum downwind distance of the 5% contour continued to move downwind for an additional 10 to 20 s after the spill was terminated. The maximum value for both models is in good agreement with the experimental value as shown in Table 2. The GD result shown in Fig. 4(b) is a steady-state result since this model is not time dependent. The X_{LFL} value for the GD model is significantly less than the corresponding value for the other two models and the experimental result. The GD cloud width is also seen to be too narrow, just as it was in the Burro 3 and 7 results. For example, the 5% contour has a maximum width of 30 m in the GD plot while it has a 70 m width in the experimental plot. A comparison of the higher concentration levels is not possible since the RPTs significantly hampered the operation of the first row of instruments.

A view of the crosswind cloud structure is shown in Fig. 5 where the experimental results are compared to the SLAB and FEM3 results at a downwind distance of 140 m. The FEM3 model result agrees very well with the experimental plot, especially with regard to the vertical profile. The 1, 5 and 10% contours have maximum heights of 1.3, 3.3 and 8.0 m in the experimental plot and 1.3, 3.4 and 9.5 m in the FEM3 plot. As was the case with the previous examples, the SLAB model predicts too high a height for the higher contours (5 and 10%) and too low a height for the lower contours (1%). The GD model (result not shown in figure) produces a cloud which is much higher than observed in the experiment. For example, the 5% contour has a maximum height of 8.5 m and the 1% contour has a height of 15.6 m.

Any interpolation error in the experimental result for the height of the

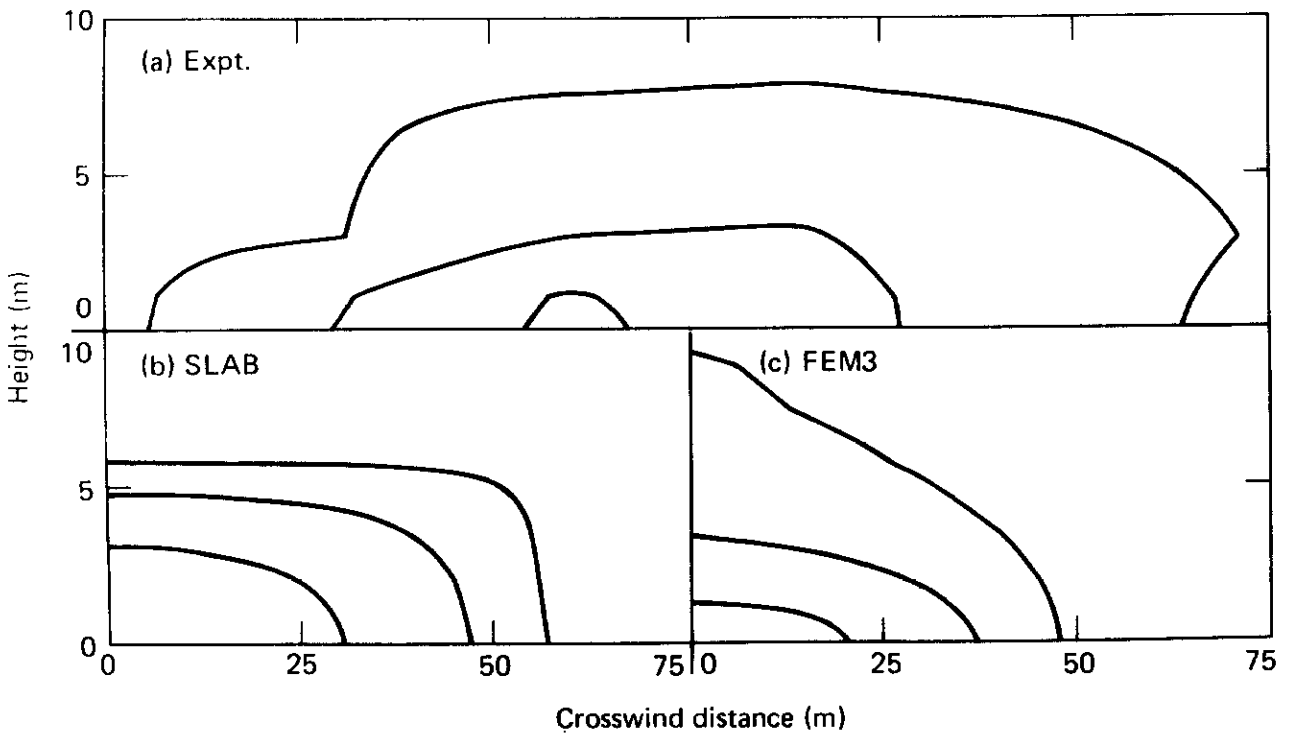

Fig. 5. Burro 9 crosswind contour plots of cloud concentration 140 m downwind at t = 70 s. Contour lines designate 1, 5 and 10% levels and vertical to horizontal distance scale is 1 to 4.

contours in Fig. 5(a) is undoubtedly quite small since these heights are very close to the heights of the instruments. If a concentration profile of $c = c_0 \exp[-(z/z_0)^n]$ is fitted to the experimental data, the power of the exponent for the best fit is found to be $n = 1.0$. This suggests that the vertical profile, at least in this case, is closer to an exponential than it is to a quadratic (used in the SLAB model) or a Gaussian (used in the GD model).

The maximum recorded concentration was always at the lowest (1 m) station in the first two rows. However, at the 400 m row, the maximum concentration measurement was observed to occur most of the time at the 3 m height, as shown in Fig. 6(a) (note, the inner contour is the 2.5% level). Neither the SLAB nor the FEM3 models predict this result (see Fig. 6) although they do predict the general height, width, and concentration level of the cloud fairly well. The SLAB model is not capable of predicting an elevated peak concentration since the vertical profile is specified to be quadratic with the peak at ground level. However, this is not the case with the FEM3 model. Several possible reasons for this discrepancy seem plausible, including insufficient heat sources to make the cloud buoyant and an inaccurate approximation to the ambient velocity profile near the ground.

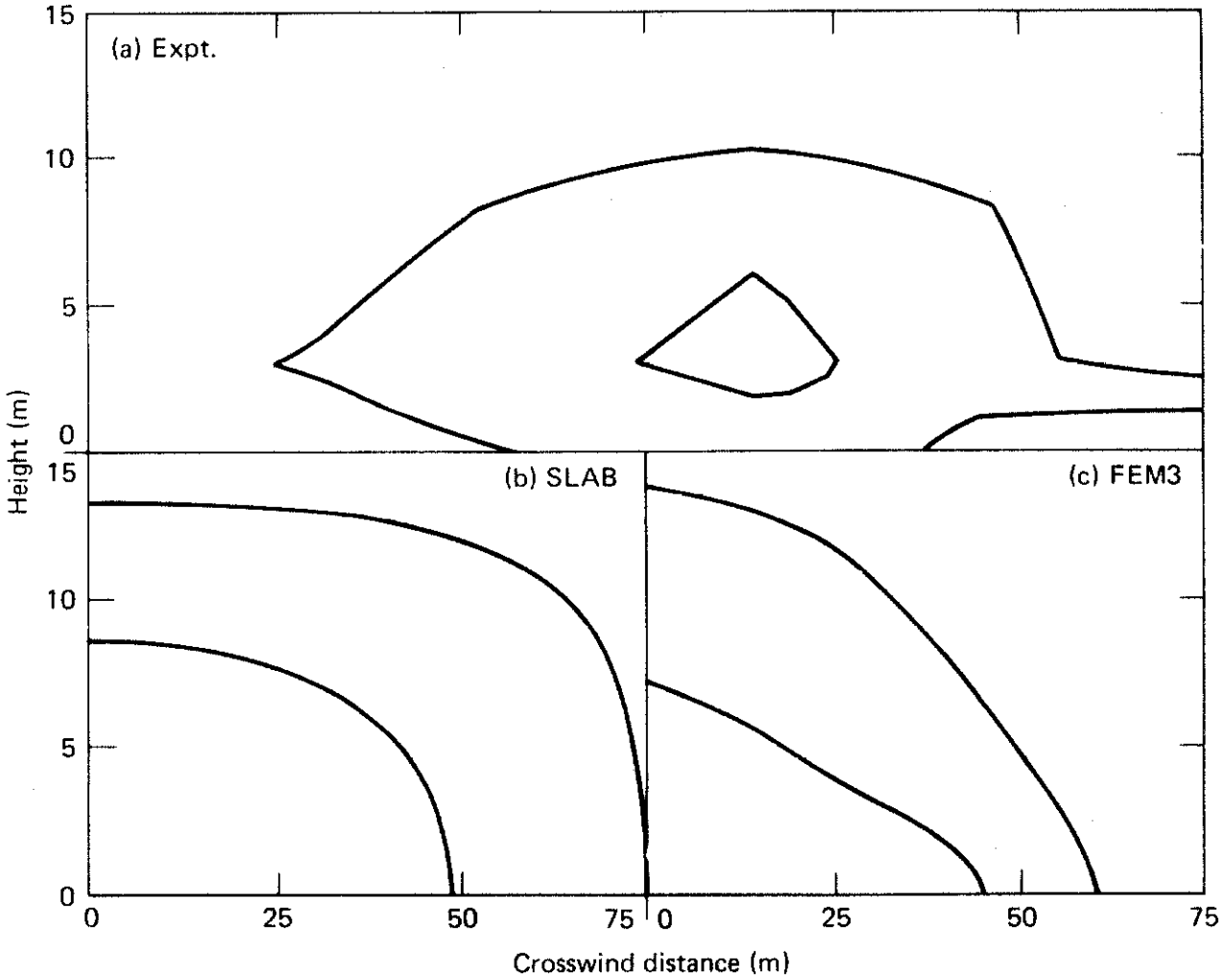

Fig. 6. Burro 9 crosswind contour plots of cloud concentration 400 m downwind at t = 120 s. Contour lines designate 1 and 2.5% levels and vertical to horizontal distance scale is 1 to 4.

4.4 Burro 8

Burro 8 was perhaps the most interesting of all the experiments. It was conducted under low wind speed and stable atmospheric conditions. The resulting vapor cloud was much wider than any of the others and it developed a very distinct bifurcated structure. It also travelled upwind and lingered over the source region for more than 100 s after the spill was terminated. This behavior can be seen in Fig. 7(a—d) which shows a time sequence of pictures of the Burro 8 vapor cloud. The visible cloud is the result of condensed water vapor and in this test is estimated to correspond to a concentration of 15—20%. In contrast to this very wide cloud, Fig. 7(e) shows a picture of the cloud observed in Burro 6 which is typical of the higher wind speed cases.

The FEM3 model ran into some difficulties in attempting to simulate the low horizontal diffusivity predicted by its turbulence submodel. Spurious oscillations due to insufficient spatial resolution in the horizontal plane began to occur about 140 s into the simulation. (Adequate spatial resolution would have required about an order of magnitude increase in mesh points.) To overcome this problem, the horizontal diffusivity was increased, and the simulation was re-run using a constant horizontal diffusivity of 2 m^2/s. The second simulation generally agreed quite well with the first run during the initial 140 s of the simulation, and is used here for times later than 140 s.

A horizontal contour plot of the cloud concentration 1 m above ground at t = 160 s is shown in Fig. 8 along with the corresponding results from the three models. The bifurcated structure, so apparent in the experimental results, is not observed in these model plots, although a bifurcated structure did occur in the FEM3 result at higher elevations and will be shown later. While the structure is different, the value of X_{LFL} at this time is just under 300 m for both lobes of the experimental result, and for both the SLAB and FEM3 model results.

The downwind distance to the LFL continued to grow for a considerable length of time after the spill was terminated at t = 106 s. The value of X_{LFL} in the experimental plots reached a maximum of 325 m and remained in the vicinity of 300 m for well up to t = 280 s. However, the actual maximum value of X_{LFL} in the lower lobe of Fig. 8(a) may have been missed since this lobe extends well beyond the edge of the array over a dry lake bed, the elevation of which is about 6 m below that of the instrument array centerline. In addition, a "puff" of vapor with a greater than 5% gas concentration entered the array from this side between 380 and 440 s and passed through the 400 m row of instruments at the 3 m level. Consequently, the maximum X_{LFL} value shown in Table 2 for this experiment is 420 m. The maximum X_{LFL} values for the GD, SLAB, and FEM3 models were 660, 418, and 630 m respectively. As noted earlier, the GD result using a higher stability class (GD+) was 1150 m, a significant overestimation. The net effect of terrain on the vapor dispersion in this experiment is difficult to quantify, although it undoubtedly did play a significant role. The presence of topographical features at the China Lake site has been shown to reduce the distance to the

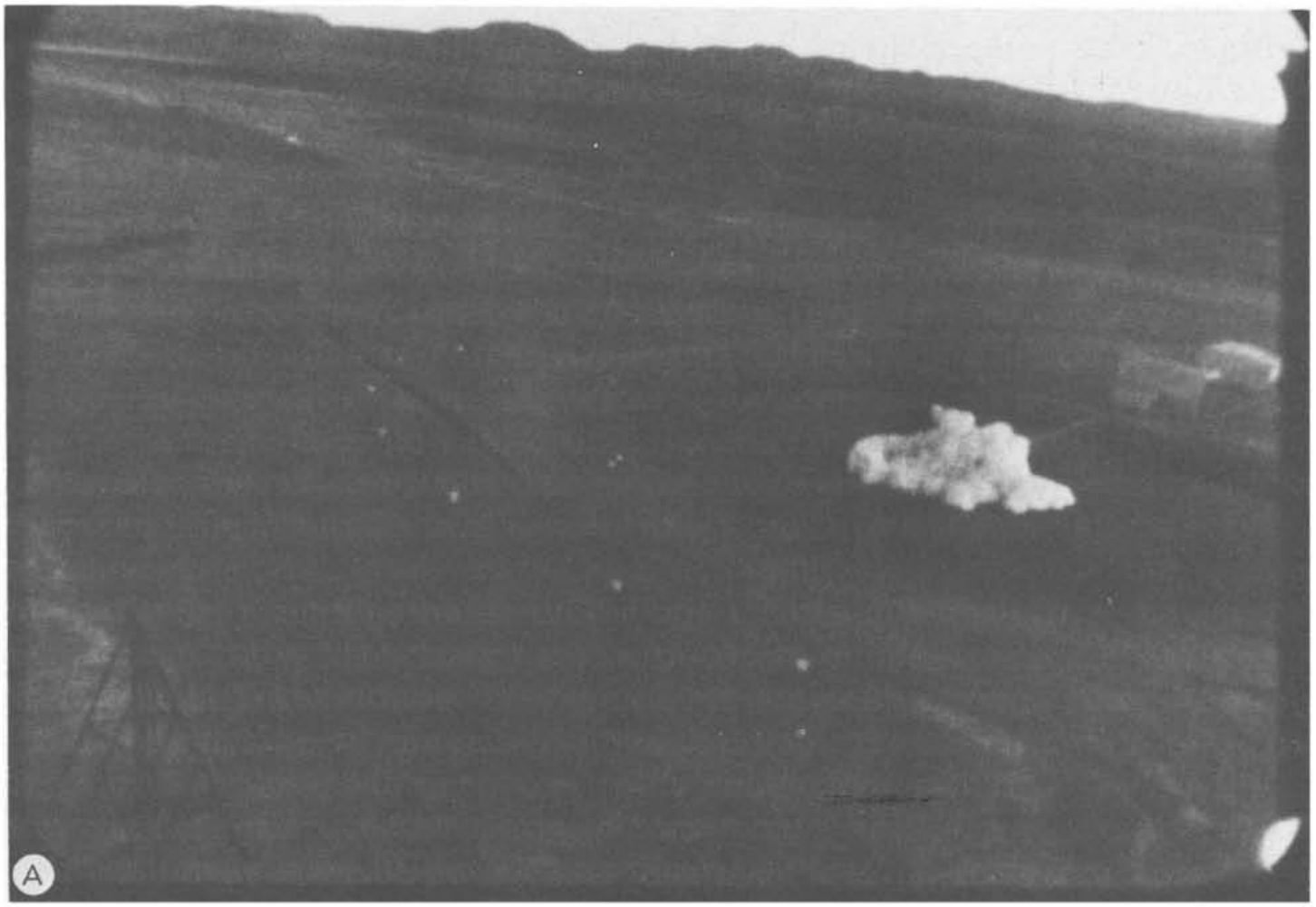
A

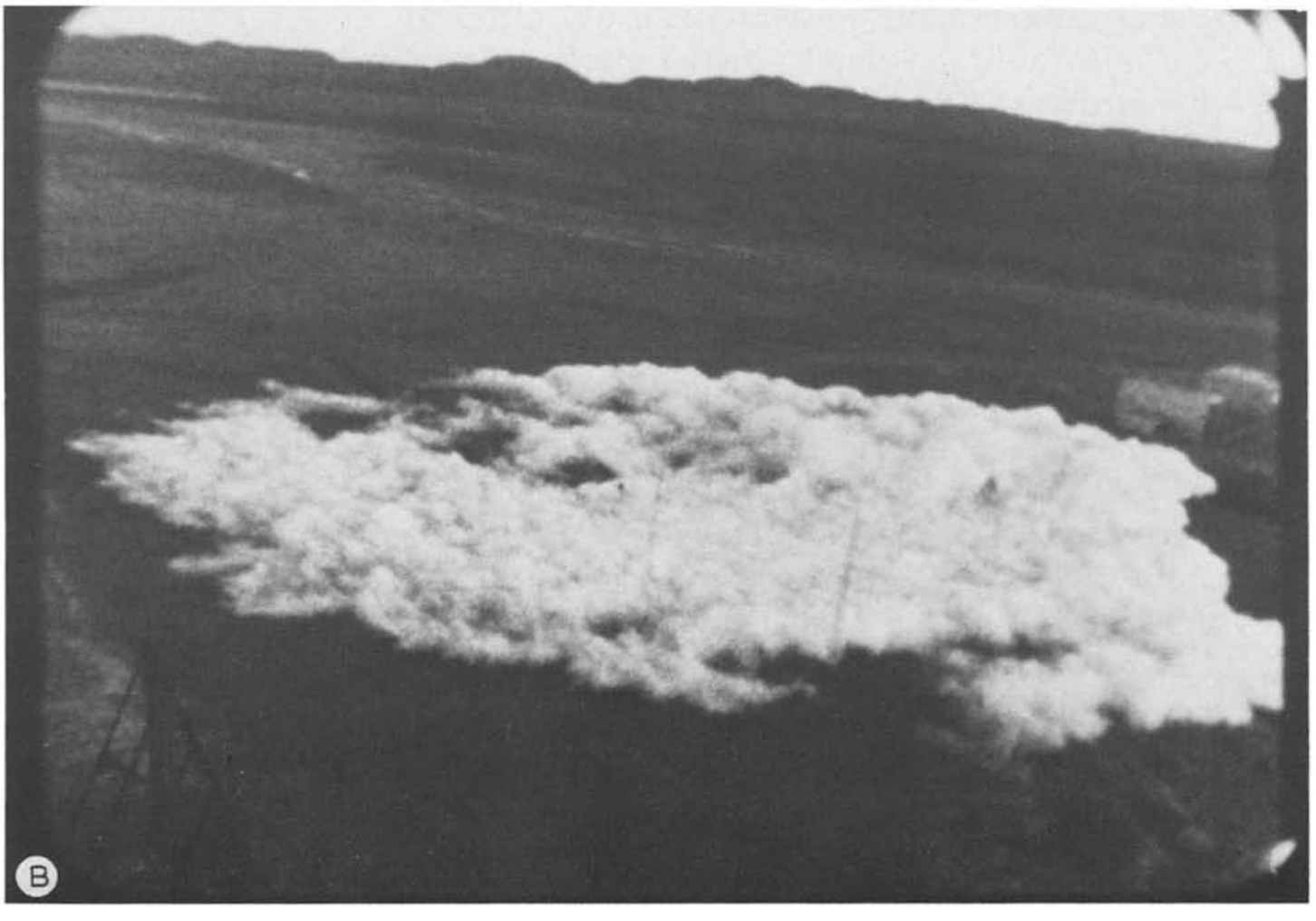
B


C


D

Fig. 7. Photographs of Burro 8 vapor cloud at (a) t = 2 s, (b) t = 30 s, (c) t = 80 s, (d) t = 160 s, (e) of Burro 6 vapor cloud after quasi-steady state had been reached. Spill rates were similar in both tests (16 m³/min in Burro 8 and 13 m³/min in Burro 6). The main difference between the two tests was the more stable atmospheric conditions and lower wind speed (1.8 m/s vs. 9.1 m/s) in Burro 8 test.

LFL in wind tunnel experiments [23], so the experimental value of X_{LFL} might have been greater if the terrain was flat. Another factor which complicates comparison of the models with experiment is changes in the ambient wind speed. In this experiment, the ambient wind speed decreased in a fairly steady fashion by about 30% over the duration of the test.

As noted earlier, the vapor cloud lingered over the source region for a considerable length of time after the LNG spill was terminated. While there were no concentration measurements within the spill pond area, we can look at when the leading and trailing edges of the cloud passed a particular row of instruments and compare the time difference to the LNG spill time. This was done for the 140 m row and the results are shown in Table 3, where the arrival and departure times of the 1% and 5% concentration levels are given. The difference between these two times is seen to be 90—260 s longer than the spill time of 106 s, depending on the concentration level and the lobe of the bifurcated cloud being considered. The SLAB and FEM3 results are also shown in Table 3. The SLAB results are in very good agreement with those for lobe 2. The good agreement at the 1% concentration level was probably

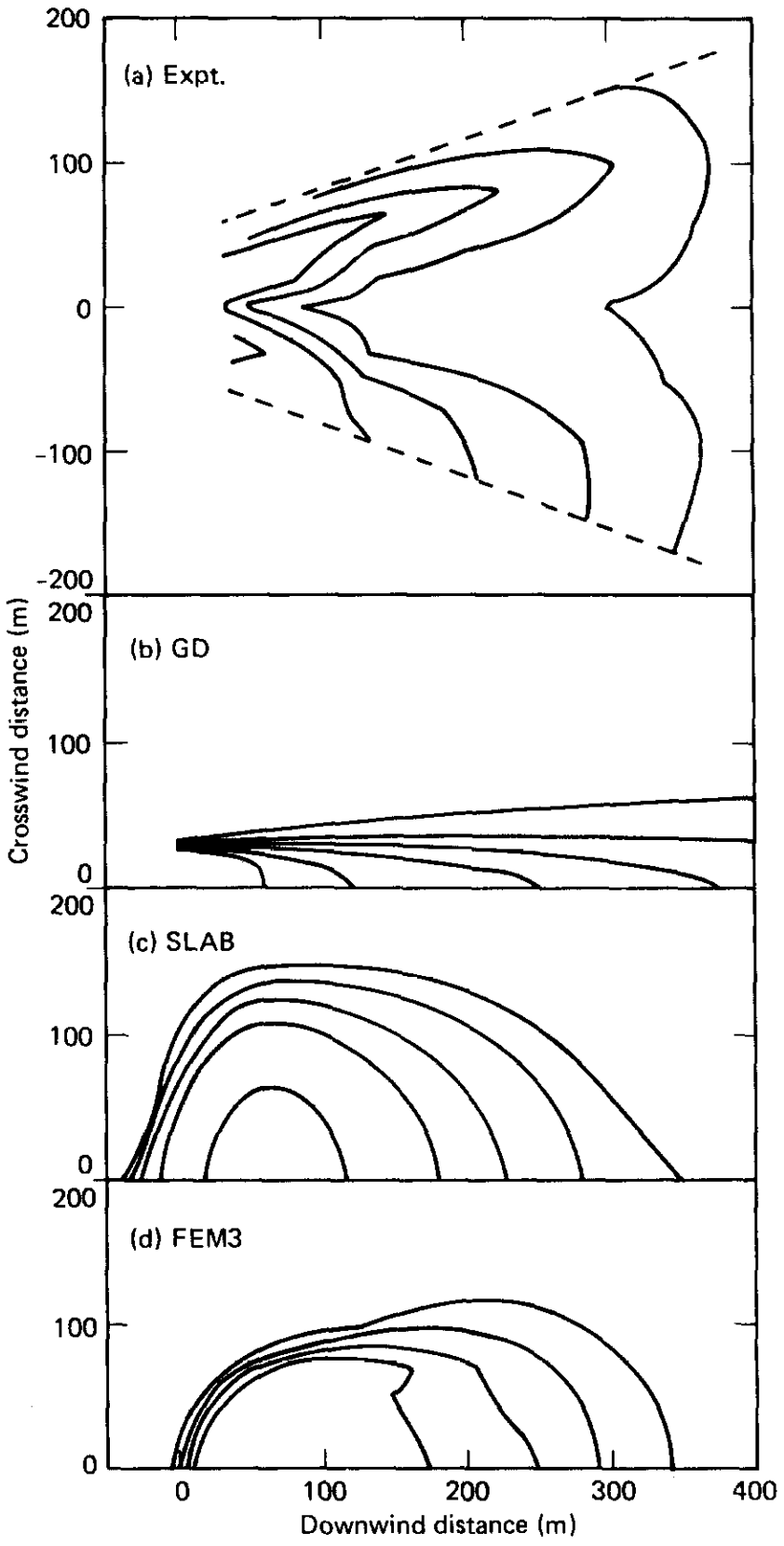

Fig. 8. Burro 8 horizontal contour plots of cloud concentration 1 m above ground at t = 160 s. Dashed lines in plot (a) indicate the outer extent of instrumentation array. Contour lines designate 1, 5, 10, 15, 25, and 35% levels and crosswind to downwind distance scale is 1 to 1.

helped considerably by the diffusion terms. These terms were added to the SLAB model to increase numerical stability, and their main effect is to broaden the leading and trailing edges. The FEM3 results for the 5% concentration level are also in good agreement with the lobe 2 results, but the trailing edge of the 1% contour does not linger behind the cloud as long as in the experiment.

TABLE 3

Burro 8 cloud arrival and departure times at the 140 m row

	Experiment			
	Lobe 1*	Lobe 2	SLAB	FEM3
Arrival time (s)				
1% concentration	55	55	55	60
5% concentration	75	75	65	65
Departure time (s)				
1% concentration	420	360	350	265
5% concentration	320	270	275	255
Departure minus arrival time (s)**				
1% concentration	365	305	295	205
5% concentration	245	195	210	190

*Lobe 1 is the lobe over the lower terrain.
**For comparison, the spill time was 106 s.

The GD model does not predict time-dependent phenomena such as the movement of the leading and trailing edges of the cloud. Looking at the steady-state prediction, the major deficiency in the GD simulation is, again, the shape of the predicted vapor cloud. As can be seen in Fig. 8(b), the GD vapor cloud is very narrow in comparison to the experiment. In contrast to this, the SLAB and FEM3 vapor clouds, shown in Figs. 8(c) and (d), are much wider and quite similar to the experiment. In comparing the SLAB and FEM3 model results with each other, the vapor cloud is seen to be significantly wider in the SLAB plot than in the FEM3 plot, especially over the first 200 m downwind where gravity spread is the major factor controlling cloud width. The actual width of the cloud in this region cannot be determined accurately since the vapor cloud extended well beyond the edges of the first two rows of instruments.

The crosswind cloud shape and structure can be seen quite well, however, in Fig. 9(a) which shows a crosswind contour plot of the cloud concentration 140 m downwind at t = 200 s. The left lobe in Fig. 9(a) appears to be somewhat larger than the right one. This is probably due to gravity and topography effects since the terrain is about 6 m lower on this side of the array than it is in the middle, as noted earlier. Figures 9(b) and 9(c) show the corresponding SLAB and FEM3 results. The SLAB cloud is very low and much wider than the FEM3 result. If one extrapolates the two lobes of the experimental plot beyond the edges of the array, it appears as though the larger left lobe is about as wide as the SLAB half-width and the smaller right lobe is about as wide as the FEM3 half-width.

The bifurcated structure of the FEM3 result is shown quite clearly in Fig. 9(c). Qualitatively, it compares fairly well with the experimental result, especially in the extended lobe region. In the region of the cloud centerline,

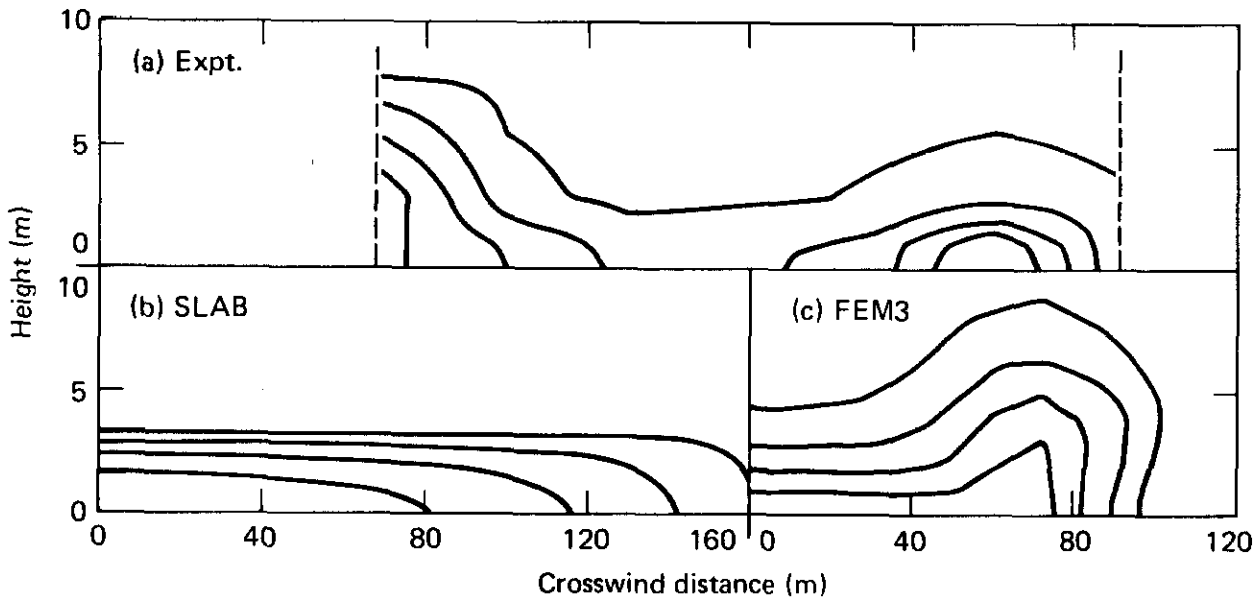

Fig. 9. Burro 8 crosswind contour plots of cloud concentration 140 m downwind at t = 200 s. Dashed lines in plot (a) indicate outer extent of instrumentation array. Contour lines designate 1, 5, 10, and 15% levels and vertical to horizontal distance scale is 1 to 6.

however, the model predicts concentrations which are too high. Consequently, the bifurcated structure is not apparent at low elevations, such as in the horizontal contour plot of Fig. 8 (d) at 1 m height. Besides accounting for terrain effects, improvements in the turbulence sub-model and more accurate treatment of the velocity profile near the ground are believed to be necessary for more quantitative agreement with experiment.

The bifurcated structure of the concentration distribution is shown in the FEM3 simulations to be due to a crosswind eddy which develops as a result of gravity spreading of the denser-than-air LNG vapor cloud. One might suspect that the crosswind gravity spread velocities in the Burro 8 test were significantly larger than those in the other experiments; however, this does not appear to be the case. Figure 10 compares FEM3 calculations of typical crosswind velocity plots for both (a) Burro 8 and (b) Burro 9 at a downwind distance of 140 m. While the eddy is much wider in the Burro 8 case, the velocities are quite similar. In both simulations, maximum crosswind velocities ranged from about 0.5 to 0.9 m/s during the time the vapor cloud passed this downwind distance. The major difference between the two velocity fields appears to be the magnitude of the downwind components. In Burro 8, the downwind velocity is only about twice as large as the maximum crosswind gravity spread velocity, while in Burro 9 (and also Burro 3 and 7), the downwind velocity is at least six times as large as the maximum crosswind gravity spread velocity. Consequently, the bifurcated concentration structure observed in Burro 8 is not due to a larger gravity spread velocity in this experiment. Rather, it appears to be the result of a higher ratio between the gravity spread velocity and the downwind velocity.

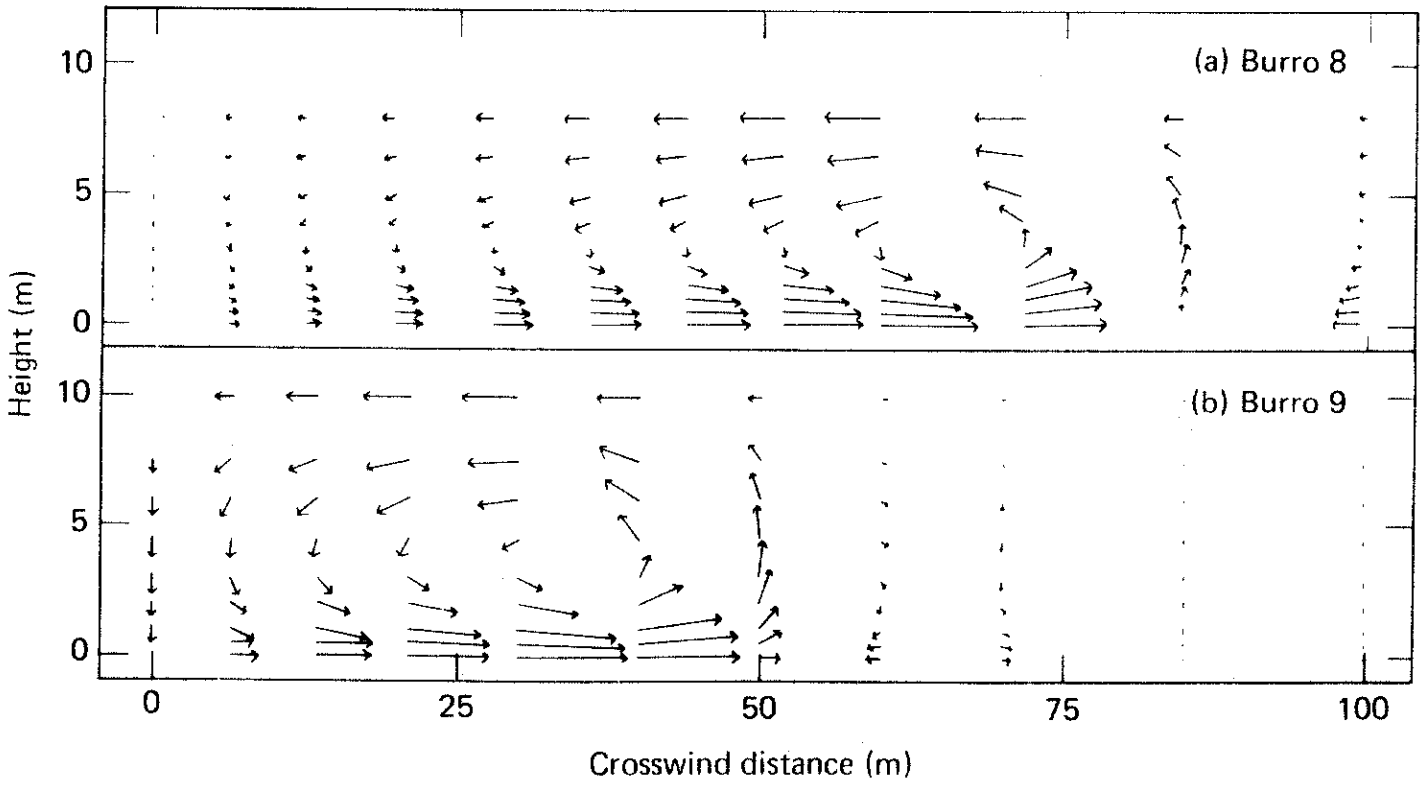

Fig. 10. Typical crosswind velocity plots 140 m downwind for (a) Burro 8 and (b) Burro 9 as calculated by FEM3 model. Maximum crosswind velocity in both cases is about 0.9 m/s. Vertical to horizontal distance scale is 1 to 2.

5. Discussion and conclusions

The range of applicability of any particular model generally depends on the degree to which important physical phenomena are approximated. Of the three models used in this study, the FEM3 model is the least limited by various approximations and restricting assumptions, and it did indeed provide the best overall description of LNG vapor cloud dispersion as observed in the four experiments addressed here. Predictions of the vapor concentration distribution in time and space over the range from 5% to 15% (the LNG flammability limits) were generally quite good. Estimates of the maximum distance to the LFL were also quite good or at least conservative (overestimated X_{LFL}).

A major accomplishment of the FEM3 model was the prediction of the bifurcated structure of the very wide vapor cloud in Burro 8. This behavior was observed in only this one experiment, which occurred under low wind speed and stable atmospheric conditions. Neither of the other two models could have reproduced this behavior since the shape of the crosswind concentration distribution was prescribed in these models and not subject to change by the conditions in the cloud. The FEM3 simulation not only predicts this behavior, but also provides the necessary information to understand how it is generated by the crosswind gravity spread vortex flow. Additional model simulations would provide more insight into the atmospheric and spill conditions under which this phenomenon would be expected to occur. For more quantitative agreement with experiment, improvements are needed in the turbulence sub-model, the approximations for the velocity

profile near the ground, and the treatment of terrain. The numerical difficulties associated with low turbulence levels must also be addressed.

From a safety point of view, it is important to be able to predict how long the vapor cloud will remain hazardous. In this regard, both the FEM3 and SLAB models accurately predicted the lingering of the vapor cloud over the source region after the spill was terminated in the low wind speed, Burro 8 test. Their ability to make this prediction was due to the inclusion within these models of the fundamental principle of momentum conservation in the wind direction. The GD model, and most other simple models, do not include these momentum effects, but simply assume that the vapor cloud travels downwind with the ambient wind speed. As shown by the Burro 8 test, this assumption can lead to a significant underestimation of the time for cloud dispersal.

The SLAB model also provided a fairly good description of the observed concentration distribution and good estimates of the maximum distance to the LFL. The excellent prediction of X_{LFL} in Burro 8 is very encouraging; however, we are cautious that this agreement might be somewhat fortuitous. If the China Lake terrain significantly reduced X_{LFL} from what it would be under flat terrain conditions, then the SLAB estimate will prove to be too short. Obviously, additional experiments under low wind speed conditions and over flat terrain are needed to verify the models in this range of atmospheric conditions.

Assuming a crosswind concentration profile for the SLAB model greatly facilitated comparison with the experimental contour plots. The quadratic vertical profile with peak concentration and zero gradient at the ground was most applicable to the Burro 8 experiment where the vapor cloud was nearly a uniform layer close to the ground. However, in the higher wind speed experiments, the concentration gradient was much steeper near the ground, and an exponential profile might be more appropriate under these conditions. If a profile is assumed, it would be preferable to incorporate this assumption into the derivation of the basic conservation equations rather than just apply it after the species equation is solved, as was done here. In this regard, a profile, the shape of which could vary with changes in the cloud properties (such as going from negative to positive buoyancy) would also be desirable; however, this might be exceeding the limits of the model. It would probably be more profitable to try to improve the main sub-models such as the entrainment, surface heat flux, and friction submodels.

The GD model estimates of the vapor cloud concentration distribution were significantly poorer than those of the other two models. In all four simulations, the predicted cloud was roughly twice as high and twice as narrow as in the experiments. The main reason for this is that the GD model includes gravity effects only in the initial calculation of the vapor source height and width, but does not include gravity effects on the subsequent downwind dispersion of the vapor cloud.

This discrepancy in cloud shape between the GD model results and the experiments illustrates the importance of gravity spread on the crosswind

concentration distribution, even when the wind speed is high and turbulence within the cloud is dominated by the ambient atmospheric conditions. In the three high wind speed simulations (Burro 3, 7, and 9), the initial GD gravity spread calculation did not even increase the width of the vapor source, since the ambient wind speed was greater than the calculated gravity spread velocity. Consequently, these GD simulations were equivalent to Gaussian plume calculations for a trace release of a neutrally buoyant emission. Neglecting the effects of gravity on the denser-than-air cloud results in a predicted vapor cloud which is much too high and too narrow, even under strong wind speed conditions.

In the model simulations, the maximum distance to the LFL is quite sensitive to the turbulence level. For example, in the GD model, turbulence level is controlled by specifying the stability class. Increasing the stability class in effect lowers the turbulence level. When the stability was increased by just one class, the value of X_{LFL} increased by 40 to 75%, depending on the initial stability category and the LNG spill rate. Similar results were found using the FEM3 model. In these calculations (not previously shown), the LNG vapor source rate was similar to that in the Burro experiments and a constant diffusivity with a wind speed of 4 m/s was used. When the vertical diffusivity was decreased from 0.5 to 0.2 m^2/s, with a similar decrease in the horizontal diffusivity, the steady state value of X_{LFL} increased by a factor of two, showing considerable sensitivity to the turbulence level.

It is interesting to note that the turbulence level, as calculated by the FEM3 turbulence sub-model equation, returned to a value quite close to the ambient level within only a few tens of metres from the LNG vapor source, even for Burro 8. This suggests that the turbulence level over a significant portion of the vapor cloud may be fairly close to the ambient level, even though gravity effects on cloud width and height are still important at these downwind locations. However, this has not been confirmed by comparison with experimental data.

With regard to the vapor source, the effective LNG evaporation rate and, in turn, the radius of the liquid pool and vapor source have remained fairly uncertain in field-scale LNG spill tests on water where the liquid pool radius is not confined. Recent analysis of IR data taken during Burro 9 suggests that the liquid LNG pool was only 5 m in radius. This implies an effective evaporation rate which is 10 times as great as the value assumed in this study and, therefore, vapor source radii which are 1/3 as large as those used in these model simulations. It should be noted that there is considerable uncertainty surrounding this observation, especially in light of the numerous RPT explosions which occurred during this experiment. The effect of such an increase in the evaporation rate on the model predictions has not been thoroughly analyzed. While the source radius would decrease by a factor of 1/3 as noted above, the overall evaporation rate (mass/time) would remain the same and be equal to the LNG spill rate (assuming the liquid pool rapidly reaches a quasi-steady state). Clearly, the effect on cloud concentration will

be greatest in the high concentration regions surrounding the vapor source and will decrease with distance from the liquid pool.

This comparison of three dense-gas dispersion models of varying levels of sophistication with the results from the Burro series of LNG dispersion experiments has provided considerable insight into the strengths and weaknesses of the three different types of models and has identified important model components that require improvement. The comparison of cloud structure between the three-dimensional, conservation equation model, FEM3, and the experiments, was generally quite good. In particular, the FEM3 prediction of a bifurcated cloud structure in Burro 8 was very encouraging. The one-dimensional, averaged conservation equation model, SLAB, also compared fairly well with experiment, especially in the prediction of the maximum distance to the LFL. In contrast to the other two models, the modified Gaussian plume model, GD, compared rather poorly with the observed cloud structure.

The experiments used in this study were performed over a limited range of spill scenarios. Consequently, additional comparisons with well-instrumented, large-scale experiments are needed in order to evaluate each model's ability to accurately simulate very large spills over a broad range of atmospheric conditions. In this regard, recent Shell LNG and propane spill experiments conducted at Maplin Sands, Gt. Britain [24] and additional LNG experiments currently underway at China Lake, California, will be most helpful.

6. Acknowledgments

The authors are indebted to all of those who participated in the Burro Series of LNG spill experiments. We would especially like to thank R.P. Koopman, R.T. Cederwall, and H.C. Rodean for their many helpful discussions regarding the data obtained in these experiments. We also wish to thank E.J. Kansa for his advice in applying boundary conditions in the SLAB and FEM3 models and D.J. Bergmann for running the GD computer simulations. This work was performed under the auspices of the U.S. Department of Energy by the Lawrence Livermore National Laboratory under Contract No. W-7405-Eng-48.

References

1 R.P. Koopman, Burro Series Data Report; LLNL/NWC 1980 LNG Spill Tests, Lawrence Livermore National Laboratory Report UCID-19075, June 1981.
2 R.T. Cederwall, D.L. Ermak, H.C. Goldwire, Jr., R.P. Koopman, J.W. McClure, T.G. McRae, D.L. Morgan, H.C. Rodean, and J.H. Shinn, Description and analysis of Burro series 40-m^3 LNG Spill Experiments, Lawrence Livermore National Laboratory Report UCRL-86704, Oct. 1981.
3 D.S. Burgess, J. Biordi, and J. Murphy, Hazards of spillage of LNG into water, U.S. Bureau of Mines, NTIS AD 754498, 1972.
4 G.F. Feldbauer, J.J. Heigl, W. McQueen, R.H. Whipp, and W.G. May, Spills of LNG on water — vaporization and downwind drift of combustible mixtures, Esso Research and Engineering Company Report No. EE61E-72, Nov. 1972.

5 P.P.K. Raj and A.S. Kalelkar, Assessment models in support of the hazards assessment handbook (CG-446-3), NTIS AD 776617, Jan. 1974.
6 A.P. van Ulden, On the spreading of a heavy gas released near the ground, Proceedings 1st International Symp. on Loss Prevention and Safety Promotion in the Process Industries, Delft, Netherlands, 1974, pp. 221—226.
7 A.E. Germeles and E.M. Drake, Gravity spreading and atmospheric dispersion of LNG vapor clouds, 4th International Symp. on Transport of Hazardous Cargoes by Sea and Inland Waterways, Jacksonville, FL, Oct. 1975.
8 J.A. Fay and D.H. Lewis, Jr., The inflammability and dispersion of LNG vapor clouds, 4th International Symp. on Transport of Hazardous Cargoes by Sea and Inland Waterways, Jacksonville, FL, Oct. 1975.
9 W.G. England, L.H. Teuscher, L.E. Hauser and B. Freeman, Atmospheric dispersion of liquefied natural gas vapor clouds using SIGMET, a three-dimensional, time-dependent, hydrodynamic computer model, Heat Transfer and Fluid Mechanics Inst., Washington State University, June 1978.
10 J.A. Havens, An assessment of predictability of LNG vapor dispersion from catastrophic spills onto water, J. Haz. Mat., 3 (1980) 267.
11 S.T. Chan, P.M. Gresho, R.L. Lee, and C.D. Upson, Simulation of three-dimensional, time-dependent, incompressible flows by a finite element method, Proc. of the AIAA 5th Computational Fluid Dynamics Conf., Palo Alto, CA, June 1981.
12 S.T. Chan, P.M. Gresho and D.L. Ermak, A three-dimensional, conservation equation model for simulating LNG vapor dispersion in the atmosphere, Lawrence Livermore National Laboratory Report UCID-19210, Sept. 1981.
13 R.A. Cox and R.J. Carpenter, Further development of a dense vapor cloud dispersion model for hazard analysis, Symp.: Schwere Gase, Battelle-Institute, Frankfurt am Main, Sept. 1979.
14 K.J. Eidsvik, A Model for Heavy Gas Dispersion in the Atmosphere, Atm. Env., 14 (1980) 769.
15 O. Zeman, The dynamics and modeling of heavier-than-air cold gas releases, Lawrence Livermore National Lab. Report UCRL-15224, April 1980, Atmos. Environ., 16 (4) (1982) 741—751. See also: O. Zeman, Parameterization of the dynamics of stable boundary layers and nocturnal jets, J. Atmospheric Sci., 36 (1979) 792; O. Zeman, Progress in the modeling of planetary boundary layers, Annual Review of Fluid Mechanics, 13 (1981) 263.
16 G.W. Colenbrander, A mathematical model for the transient behavior of dense vapor clouds, 3rd International Symp. on Loss Prevention and Safety Promotion in the Process Industries, Basle, Switzerland, Sept. 1980.
17 F.A. Gifford, Jr., Use of routine meteorological observations for estimating atmospheric dispersions, Nuclear Safety, 2 (1961) 47.
18 H. Kato and O.M. Phillips, On the Penetration of a Turbulent Layer into Stratified Fluid, J. Fluid Mechanics, 37 (1969) 643.
19 N.K. Madsen and R.F. Sincovec, ALGORITHM 540 PDECOL, General collocation software for partial differential equations, ACM Trans. on Mathematical Software, 5 (1979) 326.
20 Y. Ogura and N. Phillips, Scale analysis of deep and shallow convection in the atmosphere, J. Atmospheric Sci., 19 (1962) 173.
21 D.B. Turner, Workbook of atmospheric dispersion estimates, U.S. Department of Health, Education and Welfare, PB-191 482, 1970.
22 D. Golder, Relations among stability parameters in the surface layer, Boundary-Layer Meteorology, 3 (1972) 47.
23 D.E. Neff and R.N. Meroney, Dispersion of vapor from LNG spills-simulation in a meteorological wind tunnel of spills at China Lake Naval Weapons Center, CA, Colorado State University Report CER78-79DEN-RNM41, 1979.
24 D.R. Blackmore, J. Eyre, J.B. Homer, and J.A. Martin, Refrigerated gas safety research, American Gas Association Transmission Conf., Atlanta, GA, May 1981.